catalysts

MDPI

Article

Synergistic Cu-Pd Nanocatalysts on MOF-Derived N-Doped Carbon for Selective Hydrogenolysis of Lignin to Aromatic Monomers

Wenjun Lei, Yan Fu, Shipeng Gu, Shuaishuai Qiu and Jie Chang *

School of Chemistry and Chemical Engineering, South China University of Technology, Guangzhou 510640, China; 202320123882@scut.edu.cn (W.L.); fuyan@scut.edu.cn (Y.F.); 202320123326@scut.edu.cn (S.G.); qss13298180884@163.com (S.Q.)
* Correspondence: changjie@scut.edu.cn

Abstract: Catalytic hydrogenolysis of lignin to produce high-value monophenols has emerged as a pivotal strategy in modern biorefineries. In this study, we synthesized spherical nitrogen-doped porous carbon (SNCB) materials by using Al/Co-BTC as a precursor, introducing melamine as a supplementary carbon and nitrogen source, and activating the material with NaOH solution. The SNCB framework was decorated with Cu-Pd bimetallic nanoparticles, exhibiting outstanding catalytic activity in the hydrogenolytic depolymerization of organosolv lignin. The Cu-Pd@SNCB catalyst exhibited remarkable activity, attributed to the hierarchical porous structure of SNCB that facilitated metal nanoparticle dispersion and reactant accessibility. The synergistic effect between Cu as the reactive site for reactant adsorption and Pd as the reactive site for H_2 adsorption enhanced the catalytic activity of the catalyst. Systematically optimized conditions (2 MPa H_2, 270 °C, 3 h) yielded 43.02 wt% phenolic monomers, with 4-(3-hydroxypropyl)-2,6-dimethoxyphenol dominating the product profile at 46.3% selectivity. The catalyst and its reaction products were analyzed using advanced characterization techniques, including XPS, XRD, TEM, SEM, BET, GC-MS, GPC, 2D HSQC NMR, and FT-IR, to elucidate the reaction mechanism. The mechanism proceeds through: (1) nucleophilic substitution of the β-O-4 hydroxyl group by MeOH, followed by (2) simultaneous hydrogenolytic cleavage of C_β-O and C_α-O bonds mediated by Cu-Pd@SNCB under H_2 atmosphere, which selectively produces 4-(3-hydroxypropyl)-2,6-dimethoxyphenol and 4-propyl-2,6-dimethoxyphenol. This study proposes a bimetallic synergistic mechanism, offering a general blueprint for developing selective lignin valorization catalysts.

Keywords: lignin; hydrogenolysis; bimetallic catalyst; phenolic monomers

check for updates

Academic Editor: Carolina Belver

Received: 12 April 2025
Revised: 3 May 2025
Accepted: 4 May 2025
Published: 7 May 2025

Citation: Lei, W.; Fu, Y.; Gu, S.; Qiu, S.; Chang, J. Synergistic Cu-Pd Nanocatalysts on MOF-Derived N-Doped Carbon for Selective Hydrogenolysis of Lignin to Aromatic Monomers. *Catalysts* **2025**, *15*, 455. https://doi.org/10.3390/catal15050455

Copyright: © 2025 by the authors. Licensee MDPI, Basel, Switzerland. This article is an open access article distributed under the terms and conditions of the Creative Commons Attribution (CC BY) license (https://creativecommons.org/licenses/by/4.0/).

1. Introduction

The global energy landscape has remained heavily dependent on fossil fuels, exacerbating critical challenges, including resource depletion, environmental degradation, and climate change [1,2]. Lignin is a fundamental structural component of plant cell walls, and it coexists with cellulose and hemicellulose in lignocellulosic biomass. Comprising 15–30 wt% of lignocellulosic biomass, lignin ranks as the second-most abundant renewable aromatic polymer on Earth, surpassed only by cellulose in natural abundance [3]. As one of the most promising biomass feedstocks, lignin can be efficiently converted to produce green fuels, high-value chemicals, and functional materials [4,5]. Phenolic monomers are currently produced industrially from petroleum-based feedstocks through energy-demanding processes, creating dual challenges of resource unsustainability and substantial

environmental burdens. The structural complexity of lignin arises from cross-linked phenylpropane units (guaiacyl/syringyl/*p*-hydroxyphenyl) linked via C-O and C-C bonds [6,7]. Selective cleavage of lignin's interunit linkages through catalytic depolymerization offers a sustainable route to transform renewable biomass into platform chemicals, potentially replacing petroleum-derived analogues [8,9].

Recent advances in lignin valorization have focused on its conversion to monomeric phenols, with significant progress having been reported in the past decade [10]. Multiple catalytic approaches include acid/base-catalyzed cleavage, oxidative depolymerization, and hydrogenolytic conversion, each offering distinct reaction pathways. Among these methods, hydrogenolysis stands out due to its superior product value, moderate reaction conditions, excellent selectivity, and environmental compatibility [11]. Extensive catalyst development has yielded various metal-based systems for lignin hydrogenolysis, spanning noble and non-precious metals [12]. Noble metal catalysts (Pd, Pt, Ru, Au) supported on diverse carriers achieve phenolic monomer yields of 15–55 wt%, confirming their effectiveness [13–17]. However, the high cost of precious metals limit their industrial-scale applications [18,19]. This challenge has driven the development of bimetallic systems, where non-precious metal doping not only reduces cost but also creates synergistic effects that enhance catalytic activity, selectivity, and stability [20–22].

Bimetallic catalysts consistently demonstrate superior performance over monometallic counterparts in lignin hydrogenolysis due to synergistic intermetallic effects. Studies have shown that Ni-Ru bimetallic systems enhance Lewis acidity by 40–60%, promoting electron transfer for selective C-C/C-O bond cleavage in straw lignin, with reported monophenol yields reaching 19.5% [23]. Similarly, Ni-Pd catalysts have exhibited 2.3-fold higher activity compared to monometallic systems in birch lignin hydrogenolysis, achieving 37.2 wt% phenolic monomer yield at 245 °C within 4 h, which is attributed to metal synergy [24]. Notably, Fe-Pd/HZSM-5 catalytic systems have demonstrated 27.92% aromatic yield under conditions of 320 °C, 2 h, and 1 MPa H_2 in ethanol-water solvent, where Fe incorporation was found to reduce Pd particle size by 35–50% while inducing dual geometric and electronic effects [25].

The strategic incorporation of non-precious metals has emerged as a cornerstone in catalytic design, enabling the development of cost-efficient alternatives to noble metal systems. Recent studies have demonstrated that Cu/Ni-MOF catalysts prepared through impregnation methods exhibit exceptional characteristics, including high metal dispersion, strong Lewis acidity, and remarkable stability [26]. Mixed oxide catalysts such as CuMgAlOx have shown particular efficacy in ethanol-mediated lignin depolymerization, achieving 23 wt% monomer yield through optimized redox and acid–base bifunctionality [27].

The periodic coordination environments characteristic of metal–organic frameworks (MOFs) facilitate precise metal center anchoring, generating well-defined active sites with precisely tuned electronic structures for targeted catalytic applications. Recent studies demonstrate that Pd nanoparticles confined within carboxyl-functionalized UiO-66 frameworks achieve exceptional catalytic performance in vanillin-to-MMP hydrogenolysis due to the combined effects of synergistic metal–support interactions and optimal pore size confinement effects [28]. Advanced catalyst systems employing N-doped porous carbon supports have been shown to stabilize ultra-dispersed Pd nanoparticles with electron-deficient properties, exhibiting 40% higher activity than conventional activated carbon supports in lignin hydrogenolysis relative to conventional carbon supports [29].

However, high loadings of precious metals increase catalyst cost, and the reaction mechanism remains to be further elucidated. In this study, we developed a Cu-Pd bimetallic catalyst supported on MOF-derived N-doped hierarchical porous carbon (Cu-Pd@SNCB) specifically designed for the valorization of eucalyptus lignin. Comprehensive characteri-

zation of the depolymerization products revealed the reaction pathways and active-site mechanisms during lignin conversion.

2. Results and Discussion

2.1. Catalyst Characterization

The preparation of Cu-Pd@SNCB is schematically illustrated in Figure 1. The catalyst morphology and metal particle distribution were characterized by scanning electron microscopy (SEM) and transmission electron microscopy (TEM). FE-SEM analysis (Figure 2a) revealed the three-dimensional porous architecture of Cu-Pd@SNCB, with exposed carbon nanosheets and irregular spherical particles (Figure S1). The highly porous structure exhibits exfoliated carbon nanosheets and predominantly irregular spherical particles, which provide enhanced surface area relative to ideal spheres. HRTEM images (Figure 2b) demonstrate uniform metal nanoparticle dispersion with no observable aggregation, consistent with the elemental mapping results (Figure S2). Figure 2c HRTEM images further characterize the microstructures of Pd, Co, and Cu; the lattice spacings are 0.220 nm, 0.202 nm, and 0.25 nm, which are attributed to the Pd (111) surface, Co (111) surface, and CuO (111) surface, respectively. The results are consistent with the XRD patterns [30]. As shown in Figure 2d, C, N, O, Pd, and Cu are uniformly dispersed. The successful loading of Pd and Cu was confirmed.

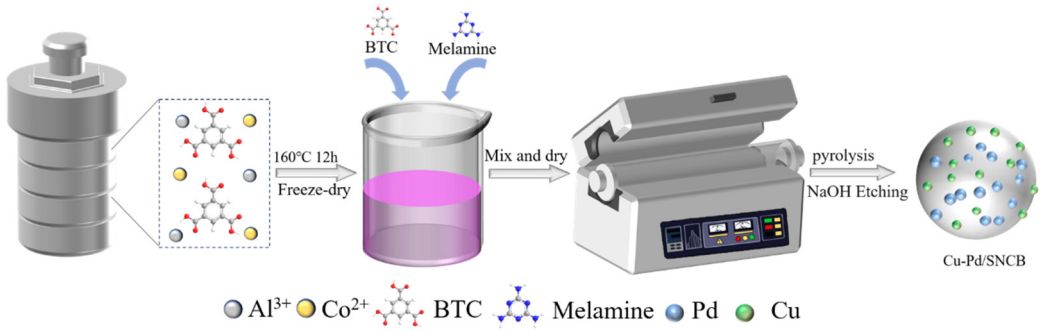

Figure 1. Schematic illustration of the preparation of Cu-Pd@SNCB.

Figure 3 presents the XRD patterns of (a) fresh Cu-Pd@SNCB, (b) recycled Rec-Cu-Pd@SNCB, and (c) Pd@SNCB reference catalyst, with Miller indices assigned according to ICDD reference databases. In Figure 3a, the characteristic XRD peak at 2θ = 46.6° is attributed to the lattice plane of Pd (200) (PDF #. 06-0681) [31]. The characteristic XRD peaks at 2θ = 35.5° and 38.7° correspond to (11-1) and (111) typical peaks of CuO (PDF #. 48-1548) [32]. The XPS confirms the oxidation of copper species in the catalyst to CuO, as evidenced by the characteristic binding energy peaks corresponding to Cu^{2+} in CuO (Figure 4c). The distinct XRD peaks at 2θ = 44° and 51° index to the (111) and (200) planes of face-centered cubic Co (PDF #. 15-0806), confirming the thermal reduction to metallic cobalt [33]. Compared to curve (a), the peaks in curve (b) are more numerous and relatively dispersed, probably due to the partial shedding of the loaded metal during the recycling process (Figure S3). Curve (c) is compared with curve (a), whereas curve (c) does not have any distinct peaks corresponding to the characteristic peaks of CuO, indicating the successful introduction of metallic copper. In addition, the elemental content ratios of the Cu-Pd@SNCB catalyst were tested (Table S2).

The XPS binding energy of Pd@SNCB catalyst is presented in Figure 4. Figure 4a shows the spectrum of N 1s with peaks corresponding to pyridine nitrogen (397.94 eV), pyrrole nitrogen (400.22 eV), and graphitic nitrogen (403.42 eV) [34]. Among them, pyridine nitrogen is the most abundant and important. Pyridinic N species with lone-pair electrons in sp^2-hybridized orbitals facilitate strong metal-support interactions through charge transfer

coordination, as confirmed by the 0.5 eV positive shift in Pd 3d binding energy compared to metallic Pd [35]. This is due to the ability of the lone pair of electrons on the pyridine nitrogen to form a coordination bond with the metal center, thus keeping the catalyst highly active and stable in the reaction [36]. The appearance of C-N (284.5 eV) bonds in the C 1 s spectra (Figure 4b) is further evidence of the successful synthesis of synthetic nitrogen-doped carbon carriers.

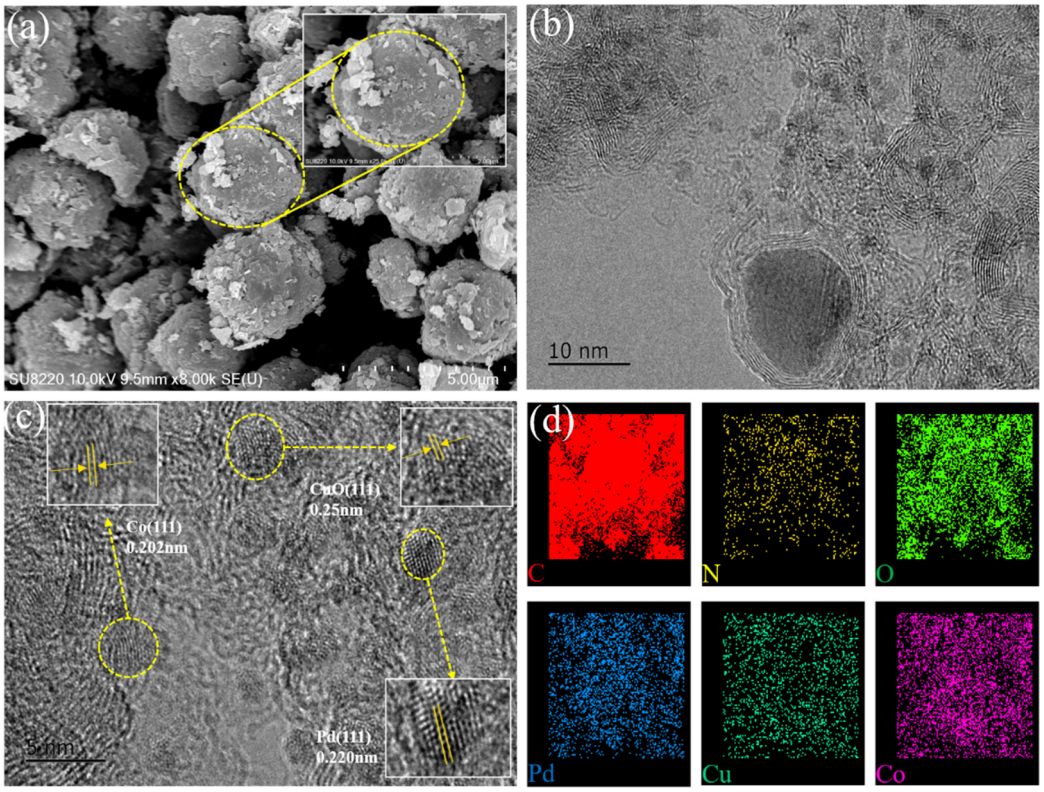

Figure 2. SEM image of catalysts: (**a**) Cu-Pd@SNCB; (**b**,**c**) high-resolution TEM images; (**d**) element mapping for C, N, O, Pd, Cu, and Co.

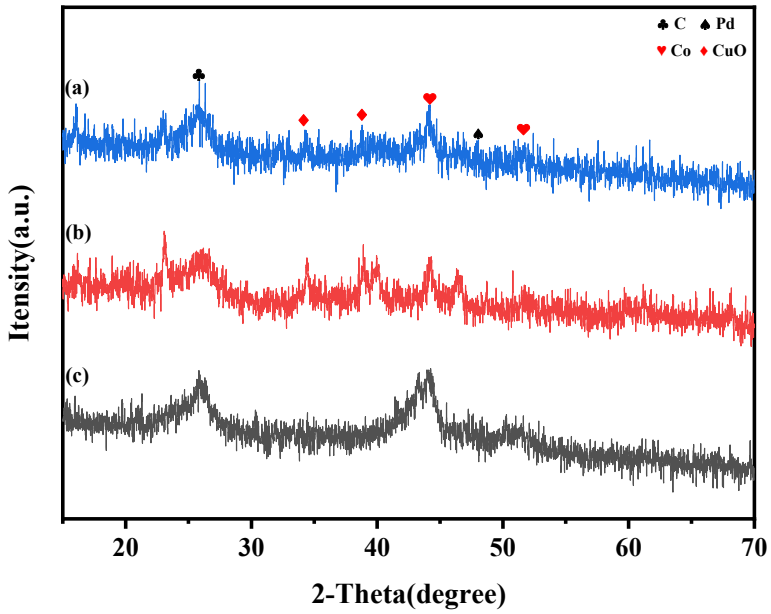

Figure 3. XRD patterns of catalysts: (a) Cu-Pd@SNCB; (b) Rec-Cu-Pd@SNCB; (c) Pd@SNCB.

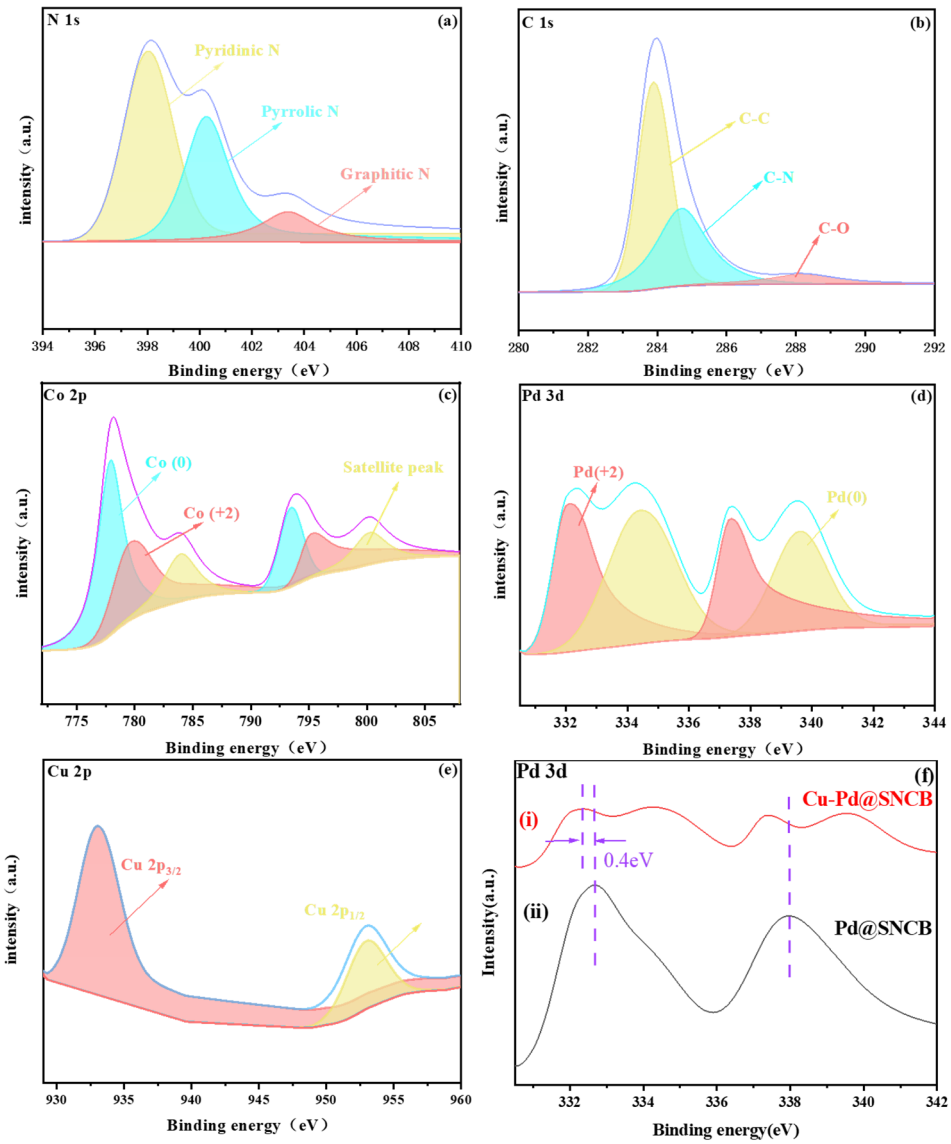

Figure 4. XPS spectrum of Cu-Pd@SNCB: (**a**) N 1s, (**b**) C 1s, (**c**) Co 2p, (**d**) Pd 3d, (**e**) Cu 2p, (**f**) Pd 3d fitting energy comparison in monometallic and bimetallic catalysts: (i) Pd@SNCB, (ii) Cu-Pd@SNCB.

The binding energies of the Pd and Co elements in the XPS spectrum were detected. The Co 2p spectrum is shown in Figure 4c. It can be observed that the two main peaks of the high-resolution mapping of the Co 2p orbitals have binding energies located near 796 eV (Co $2p_{1/2}$) and 780 eV (Co $2p_{3/2}$); specifically, the binding energy at 778.0/793.6 eV corresponds to Co, while 780.0/795.5 eV corresponds to Co^{2+} [37]. Based on the fitted spectral lines in Figure 4d, the two main peaks 339.6 eV and 334.5 eV for Pd $3d_{3/2}$ and Pd $3d_{5/2}$ were observed to correspond to Pd^0, and the binding energies of Pd^{2+} were 337.4 eV ($3d_{5/2}$) and 332.2 eV ($3d_{3/2}$) [38]. In addition, the XPS spectra of Pd@SNCB and Cu-Pd@NDCS catalysts were determined (Figure S4). The Cu 2p spectrum (Figure 4e) displays characteristic peaks at 933.12 eV and 952.97 eV, matching the reference binding energies of CuO (Cu $2p_{3/2}$: 932.82 eV; Cu $2p_{1/2}$: 952.72 eV). In addition, by comparing the Pd 3d spectra of Pd@SNCB and Cu-Pd@SNCB (Figure 4f), there exists a binding energy shift of 0.4 eV, which is due to the fact that copper atoms differ from palladium in properties such as electronegativity, and in the bimetallic system, the introduction of copper decreases the electron cloud density of palladium through electronic interactions (charge transfer). This change in electron cloud density results in a change in the adsorption capacity of

the palladium atoms on the surrounding reactants (e.g., lignin molecules, hydrogen) and in the mode of adsorption. In the hydrogenolysis of lignin, this facilitates more efficient adsorption of specific functional groups (e.g., those containing C-O bonds), promoting their activation and cleavage. The altered peak intensities (red curve) suggest that Pd atoms in the Cu-Pd bimetallic system adopt a distinct chemical state and coordination environment compared to monometallic Pd. The difference in the shapes of the peaks, on the other hand, indicates that the uniformity of the electron cloud distribution around the palladium atoms is different, and the bimetallic system may make the electron cloud distribution of palladium more favorable for the reaction. The incorporation of copper modulates Pd's electronic configuration, which enhances C-O bond adsorption in lignin through electronic effects. This Cu-Pd synergy creates distinctive catalytic sites via bimetallic cooperation. The use of bimetallic catalysts significantly improved the activity of hydrogenolysis reaction and the selectivity of phenolic compounds, reduced the occurrence of side reactions, and improved the purity and value of the products.

The Pd@SNCB and Cu-Pd@SNCB catalysts exhibited type IV N_2 sorption isotherms with H3 hysteresis loops (Figure 5), characteristic of mesoporous materials. Pore size distributions (Figure S5) confirm structural retention (<1% variation) regardless of metal loading. The hysteresis arises from capillary condensation in mesopores during adsorption versus evaporation during desorption (delayed emptying due to necking effects). This reflects the thermodynamic irreversibility described by the Kelvin equation for cylindrical pores. As shown in Figure 5, the pore size of the catalyst was mainly distributed at 3.79 nm, and the specific surface area of Cu-Pd@SNCB was 302.15 m^2/g with a pore volume of 0.36 cm^3/g. The results indicated that the high specific surface area and abundant pores of the carriers provided a prerequisite for the subsequent loading of active metals. In addition, the specific surface area of Cu-Pd@SNCB was compared with that of Pd@SNCB (Table S3).

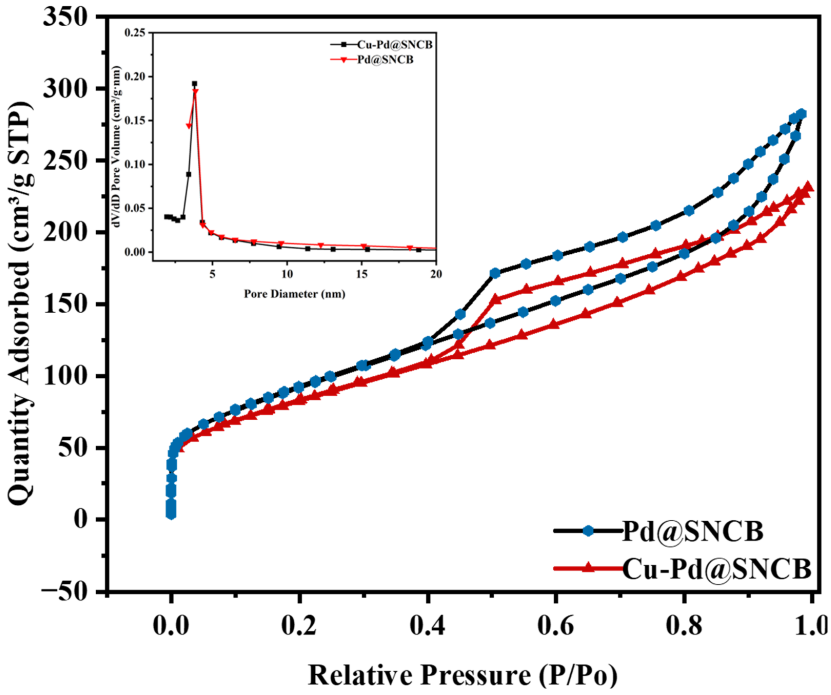

Figure 5. Cu-Pd@SNCB and Pd@SNCB N_2 adsorption isotherm and pore size distribution of catalyst.

2.2. Catalytic Hydrogenolysis of Eucalyptus Wood Lignin

The catalytic hydrogenolysis of eucalyptus wood chips was systematically investigated using the Cu-Pd@SNCB bimetallic catalyst. Lignin extraction from eucalyptus wood chips was performed using an optimized organic solvent method, achieving a purity of

94.7% as quantified by gravimetric analysis. Subsequently, catalytic hydrogenolysis of lignin was conducted at 270 °C under 2 MPa H_2 in methanol (35 mL) using 0.1 mg Cu-Pd@SNCB catalyst. The reaction yielded methanol-soluble lignin-derived oil products and a solid residue containing carbohydrate polymers and the recovered catalyst. Notably, GC-MS analysis revealed four predominant monomeric phenolic compounds: 4-n-propanol guaiacol (S1, 19.89 wt%), 4-n-propyl guaiacol (S2, 5.29 wt%), 4-n-propanol syringol (G1, 7.76 wt%), and 4-n-propyl syringol (G2, 1.83 wt%). A control experiment without the catalyst under identical conditions produced a dark lignin oil with significantly lower monomer yields compared to those obtained with Cu-Pd@SNCB.

To elucidate the mechanistic synergy between Cu and Pd in the hydrogenolysis reaction system, control experiments were conducted using catalysts with the same SNCB support but loaded with different metals under identical reaction conditions (270 °C, 35 mL MeOH, 3 h), which provided monomer yields of 39.4 wt%, 30.1 wt%, 43.02 wt%, and 32.40 wt%, respectively. Remarkably, the fabricated Cu-Pd@SNCB nanomaterial proved to be a highly effective catalyst for producing monophenols from eucalyptus lignin in high yields. Furthermore, compared to Pd@SNCB, the phenolic monomer yield increased (from 39.4 wt% to 43.02 wt%), attributed to the synergistic effects of the bimetallic catalyst. The incorporation of a second metal (Cu) also enhanced the liquefaction yield while significantly reducing the required amount of the noble metal Pd, offering economic advantages [39]. Through rational design, we developed a series of SNCB-supported Pd catalysts with controlled base metal integration, achieving palladium loadings below 0.5 wt% while maintaining higher catalytic efficiency.

The Cu-Pd@SNCB catalyst demonstrated remarkable selectivity for dihydrosinapyl alcohol production, which can be directly converted to dihydrosinapic acid—a key intermediate in non-steroidal anti-inflammatory drug synthesis. Furthermore, the derived monomers show promise as sustainable building blocks for bio-based polyesters, potentially displacing 28% of petroleum-derived phenols in epoxy resin formulations [40]. This study advances lignin biorefinery technologies by establishing that bimetallic synergy in catalyst design enables concurrent optimization of catalytic performance (43.02% monomer yield) and economic feasibility.

2.3. Investigation of Reaction Conditions

Systematic optimization studies were conducted to evaluate the influence of critical parameters (H_2 pressure: 0–3 MPa; temperature: 240–280 °C; time: 1–5 h) on lignin hydrogenolysis performance. Catalyst recyclability was assessed through four consecutive runs under optimized conditions (270 °C, 2 MPa, 3 h). The mean squared error of product yield or selectivity percentage is shown in Table S4.

2.3.1. Effect of Hydrogen Pressure

As shown in Figure 6a, the Cu-Pd@SNCB-catalyzed lignin hydrogenolysis reaction was systematically studied under varying hydrogen pressures (0–3 MPa) to assess its impact on catalytic performance. It was found that the yield of phenolic monomers was only 35.32 wt% and that the selectivity of major phenolic monomers was low when no external hydrogen was added. When no additional hydrogen was added, the active hydrogen could only come from the hydrogen donor methanol. Therefore, when no external hydrogen was added, the hydrogen content in the reaction was insufficient, resulting in low yield and selectivity of lignin depolymerization products. With increasing hydrogen pressure, the yield of phenolic monomers increased. Notably, the highest 43.02 wt% phenolic monomers could be obtained at a hydrogen pressure of 2 MPa, and the yields of the major monomer phenols S1 and G1 in the range of 0–2 MPa increased with the increase in hydrogen pressure. A decline

in phenolic monomer yield was observed at 3 MPa H_2 pressure, likely attributable to over-hydrogenation caused by excess reactive hydrogen species. Such a result may be due to excessive reactive hydrogen content, which leads to over-hydrogenation of the reaction.

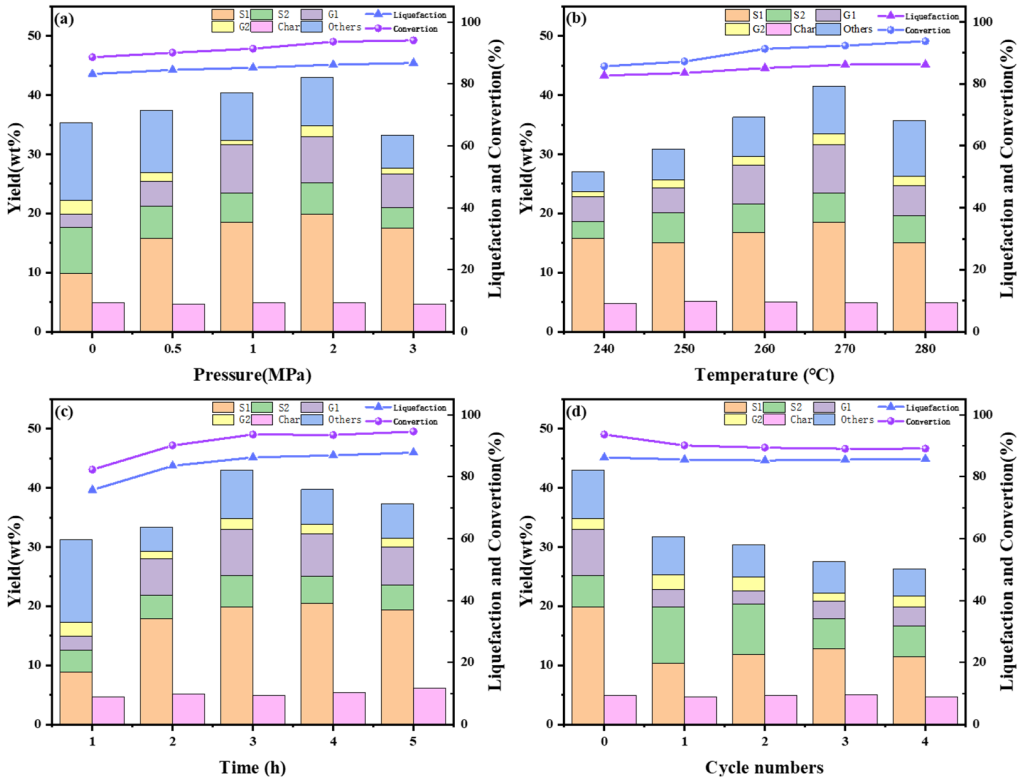

Figure 6. Effect of (**a**) H_2 pressure, (**b**) reaction temperature, (**c**) reaction time, and (**d**) cycle numbers. Reaction conditions: (**a**) 0.2 g of lignin and 35 mL of methanol, 0.1 g of Cu-Pd@SNCB, 270 °C, 3 h; (**b**) 0.2 g of lignin, 35 mL of methanol, 2 MPa H_2, 0.1 g of Cu-Pd@SNCB, 3 h; (**c**) 0.2 g of lignin, 35 mL of methanol, 2 MPa H_2, 0.1 g of Cu-Pd@SNCB, 270 °C; (**d**) 0.2 g of lignin, 35 mL of methanol, 2 MPa H_2, 0.1 g of Cu-Pd@SNCB, 270 °C, 3 h.

2.3.2. Effect of Reaction Temperature

Further optimization of reaction temperature was systematically investigated in terms of the reaction temperature for the hydrogenolysis of eucalyptus wood lignin using the Cu-Pd@SNCB catalyst. The results are shown in Figure 6b, which lists the catalytic activity of this catalyst for hydrogenolysis of eucalyptus lignin at 240–280 °C. When the reaction temperature was increased from 240 °C to 270 °C, the phenolic monomer yield sharply increased by 39.3% (from 30.89 to 43.02 wt%), and the yields of the major monomer phenols S1 and G1 demonstrated an increasing trend with the increase in reaction temperature. Reaction temperature plays a pivotal role in modulating the cleavage efficiency of lignin's interunit linkages, and within a certain range, increasing the temperature favors the hydrogenolysis of lignin. Compared with the result at 270 °C (43.02 wt%), increasing the temperature to 280 °C produced a lower yield of monomer (35.75 wt%) from the hydrogenolysis reaction, suggesting that a further increase in the reaction temperature was not favorable to the yield. This is attributed to eucalyptus lignin hydrogenolysis at 280 °C due to a change in the rate of hydrogen consumption, which triggers the repolymerization reaction. In addition, high temperatures may preferentially break less thermally stable ether bonds (e.g, β-O-4), while higher energy is required to break the remaining C-C bonds, resulting in incomplete depolymerization or an increase in by-products.

2.3.3. Effect of Reaction Time

The effect of reaction time from 1 h to 5 h on the lignin hydrolysis reaction catalyzed by Cu-Pd@SNCB catalyst was studied (Figure 6c). From the results of the study, 31.30 wt% of phenolic monomers were obtained at 1 h, which proved the effective catalytic activity of the Cu-Pd@SNCB catalyst. The optimal reaction duration of 3 h afforded the maximum phenolic monomer yield (43.02 wt%). Although lignin can achieve a certain hydrogenolysis effect at a short reaction time, the reaction time is insufficient for only some of the bonds (e.g., β-O-4 ether bonds) to be decomposed, while the more stable bonds (e.g., 5–5 carbon–carbon bonds) are not sufficiently destroyed, resulting in a residual of the macromolecular fragments and a decrease in the phenolic monomer yield. An appropriate increase in reaction time facilitated the full depolymerization of lignin. However, excessive reaction time resulted in the possible condensation of phenolic monomers to dimers or polyphenols at high temperatures or even the formation of coke, reducing the detectable monomer yield. In conclusion, the hydrogenolysis of eucalyptus wood lignin in methanol solution over Cu-Pd@SNCB catalysts was optimized for the efficient conversion of lignin to phenolic monomers at 270 °C, 3 MPa H_2, and 3 h.

2.3.4. Catalyst Cycling Performance

The ability to recover the catalyst was subsequently discussed, and at the end of the hydrogenolysis process, the catalyst was regenerated using a muffle furnace. It was roasted at 200 °C for 2 h to remove the char covering the active sites. Without any regeneration treatment, the spent Cu-Pd@SNCB was directly employed in the next catalytic run under identical optimal conditions. Figure 6d demonstrates the catalyst's cyclic stability, with the liquefaction rate dropping from 93.6% to 89.06% and phenolic monomer yield declining from 43.02% to 26.26%. The recycled catalyst was characterized by XRD, which revealed partial loss of active metals. It is noteworthy that the recycled catalyst still has clear Pd and CuO characteristic peaks but with a slight decrease in intensity.

2.4. Analysis of Products

The main components of the liquid products were determined by GC-MS. As shown in Figure 7d, the products were mainly phenolic monomers and their derivatives, which could be categorized into G-type (1, 2, 3, 4, 5) and S-type (1, 2, 3, 4, 5, 6, 7, 8). As shown in Figure 7a, the GC-MS spectra of Cu-Pd@SNCB and Pd@SNCB-catalyzed hydrogenolysis of lignin were compared, and it was seen that the peak areas of the major products of the Cu-Pd@SNCB catalyst were significantly higher than those of the Pd@SNCB catalyst, which was attributed to the synergistic effect between the bimetals to promote the hydrogenolysis of lignin. In addition, to further confirm the substance type, the pure substance 4-(3-Hydroxypropyl)-2,6-dimethoxypheno was used as a standard, and its GC-MS spectrum was examined (Figure 7b). The results demonstrated that the peak profile of the pure product was consistent with that in the product (Figure S6).

Palladium, as a platinum-group metal, demonstrates superior catalytic performance in hydrogenolysis reactions due to its exceptional hydrogen activation capability. Therefore, catalysts loaded with different active metals were subjected to controlled experiments. Comparisons were made under reaction conditions at 270 °C, 2 MPa hydrogen in MeOH for 3 h (Figure 7c), which provided 39.4 wt%, 30.1 wt%, 43.02 wt%, and 32.40 wt% monomer yields, respectively. Notably, the Cu-Pd@SNCB catalyst demonstrated the highest yield of phenolic monomers and superior selectivity toward the target product compared to the Pd@SNCB catalyst, which is attributed to the synergistic effects between copper and palladium active sites. In addition, we compared the hydrogenation products with and without the Cu-Pd@SNCB catalyst (Figure S7).

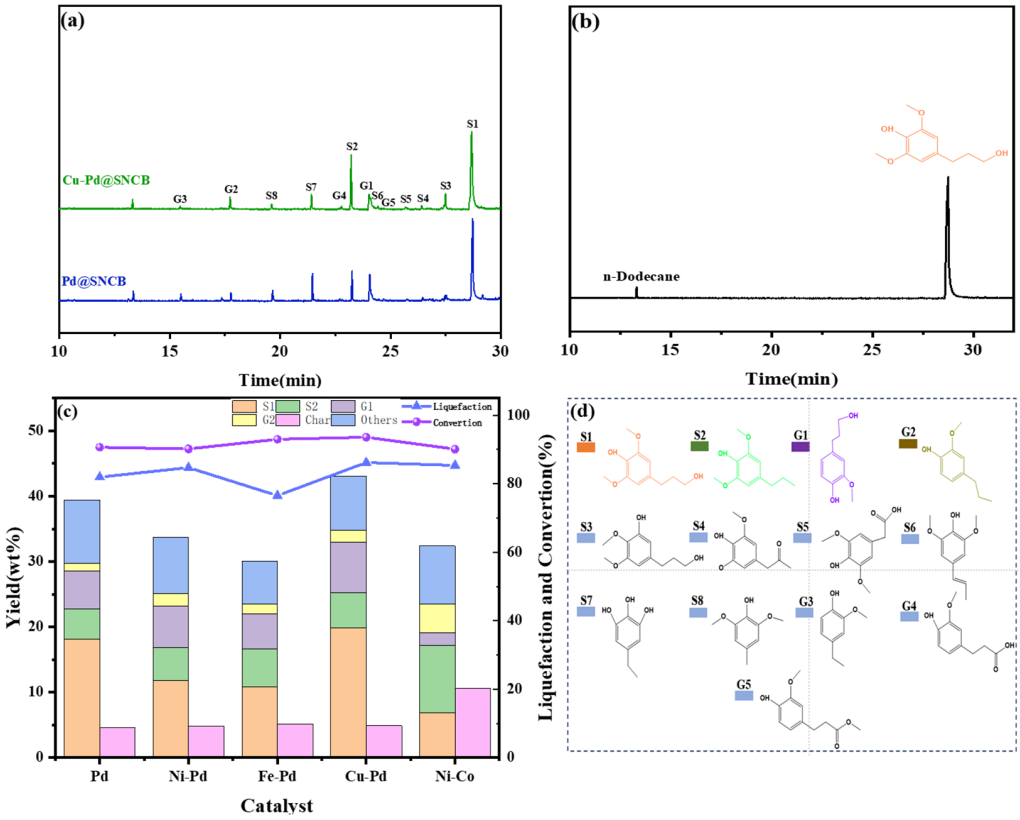

Figure 7. (**a**) GC-MS spectra in Pd@SNCB and Cu-Pd@SNCB catalytic systems. Conditions: lignin, 0.2 g; 35 mL of methanol; 2 MPa H_2; 0.1 g of the catalyst; 270 °C; 3 h. (**b**) GC-MS spectrum of 4-(3-Hydroxypropyl)-2,6-dimethoxypheno; (**c**) 0.2 g of lignin, 35 mL of methanol, 2 MPa H_2, 0.1 g of Cu-Pd@SNCB, 270 °C, 3 h. (**d**) Structures of monomers.

The gaseous products from the hydrogenolysis of lignin were characterized using GC methods to determine their composition and relative molar ratios, as shown in Table S5. High-purity hydrogen was introduced externally prior to the reaction, and the majority of the product gas at the end of the hydrogenolysis reaction was residual hydrogen. N_2 was sourced externally for residuals after purging the reactor. Decomposition of the methanol reaction medium at high temperatures and pressures may result in the appearance of CO and CO_2 gases. The C-O bond on the lignin is broken and reacts with external active hydrogen to produce CH_4. In addition, residual gases such as C_2H_6 and C_3H_8 are produced throughout the reaction.

Fourier-transform infrared spectroscopy (FT-IR) provides a non-destructive method for monitoring structural changes during lignin depolymerization. By analyzing the IR spectra of eucalyptus natural lignin (black curve) and its depolymerization products (red curve), bond-breaking mechanisms, aromatic ring modifications, and potential side reactions were revealed. FTIR analysis (Figure 8) reveals a broad absorption band at 3277–3477 cm^{-1} in natural lignin, characteristic of O-H stretching vibrations from both phenolic and aliphatic hydroxyl groups. Notably, the depolymerization products exhibit intensified O-H signals, suggesting cleavage of β-O-4 ether bonds and subsequent liberation of free phenolic hydroxyl groups. This observation correlates well with the identified phenolic monomers (guaiacol and eugenol derivatives) in the product mixture. The narrowing of the O-H bands suggests a reduction in hydrogen bonding between hydroxyl groups, further supporting the decomposition of lignin polymers [41]. Aliphatic C-H stretching vibrations (2933 and 2840 cm^{-1}), the peaks at 2933 cm^{-1} (asymmetric C-H), and 2840 cm^{-1} (symmetric C-H) peaks at 2933 cm^{-1} (asymmetric C-H) and 2840 cm^{-1} (symmetric C-H) in natural lignin

originate from methoxy (-OCH_3) and methyl (-CH_3) and methylene (-CH_2-) in aliphatic side chains. The decrease in peak intensity upon depolymerization indicates demethoxylation (-OCH_3 removal) and aliphatic chain breakage (e.g., β-O-4 bond breakage) consistent with the depolymerization pathway that generates phenolic monomers [42]. The characteristic FTIR absorptions at 1600 cm^{-1} (aromatic C=C stretching) and 1510 cm^{-1} (C-C skeletal vibration) in natural lignin confirm the preservation of guaiacyl (G) and syringyl (S) structural units. Post-reaction: the peak intensity is slightly weakened: indicating partial hydrogenation or ring-opening reactions, but the retention of aromaticity confirms that the core phenolic structure has not been over-hydrogenated to cyclohexanol derivatives. The characteristic ether bond cleavage is evidenced by peaks at 1270 cm^{-1} (G unit C-O stretching) and 1220 cm^{-1} (H unit C-O vibration), representing key lignin ether bond signatures. The significant decrease in intensity at 1270 cm^{-1} after depolymerization is direct evidence of the breaking of the β-O-4 ether bond, which is the main depolymerization pathway [43]. The 1220 cm^{-1} peak is weakened, indicating degradation of condensed C-O-C bonds (e.g, 5-5 bonds), albeit to a lesser extent due to their higher stability [44]. The 1030 cm^{-1} peak is associated with the methoxy Ar-O bond in lignin, and the reduced signal of these characteristic peaks suggests that the C-O bond was effectively cleaved during the hydrogenolysis reaction. The weak shoulder peak at 1700 cm^{-1} (assigned to C=O stretching vibrations) indicates the formation of oxidized by-products, likely aromatic ketones or aldehydes (e.g., acetovanillone) derived from side-chain oxidation. The 1700 cm^{-1} carbonyl peak corresponded to the levulinate detected by GC-MS (retention time 12.7 min), confirming some of the benzyl alcohol oxidation side effects. Concurrently, the characteristic peak at 810 cm^{-1} (C-H out-of-plane bending of para-substituted aromatics) confirms the generation of p-cresol-type monomers. Notably, broad absorptions below 800 cm^{-1} (attributed to polyaromatic C-C vibrations) suggest coke formation. These competing pathways necessitate optimized reaction kinetics to suppress undesired side reactions [45].

Comparative 2D HSQC NMR spectra (Figure 9) reveal significant structural differences in both aromatic and side-chain regions when comparing native eucalyptus lignin with the resulting oil-like products. The typical structure of eucalyptus lignin is shown in Figure 9a, and the structure of the hydrogenolysis lignin oil product is shown in Figure 9a. Notably, in the aromatic region (δC/δH = 95 − 140/6 − 8.0 ppm), a decrease in the signals of G2, G5, 6, and S2 is shown, demonstrating the successful depolymerization of lignin by this catalytic system. The side-chain ArOMe moieties remained detectable, albeit with markedly reduced signal intensity relative to the original lignin material, with the detected cross-peaks of 4-propylphenol S/G1 (labeled in orange) located at δC/δH 31.5/2.48, 34.5/1.73, and 60.2/3.40 ppm, and of S/G2 (labeled in azure); δC/δH 37.7/2.48, 24.6/1.54, and 14.13/0.88 ppm signals were attributed to the propanol chain. In addition, no signal for β-O-4 was detected, demonstrating that the Cu-Pd@SNCB catalyst dissociated the lignin sufficiently. In addition, eucalyptus lignin and hydrogenolysis product (lignin oil) were characterized by GPC. As shown in Table S6, the Mw of lignin oil obtained after hydrodepolymerization and spinodal treatment was significantly lower, and its relative molecular mass (1056 g/mol) was obviously lower than that of crude lignin (1946 g/mol), which proved that the hydrodepolymerization reaction selectively breaks some chemical bonds in the lignin, degrading the large molecules of lignin into smaller molecules, which is consistent with the NMR characterization.

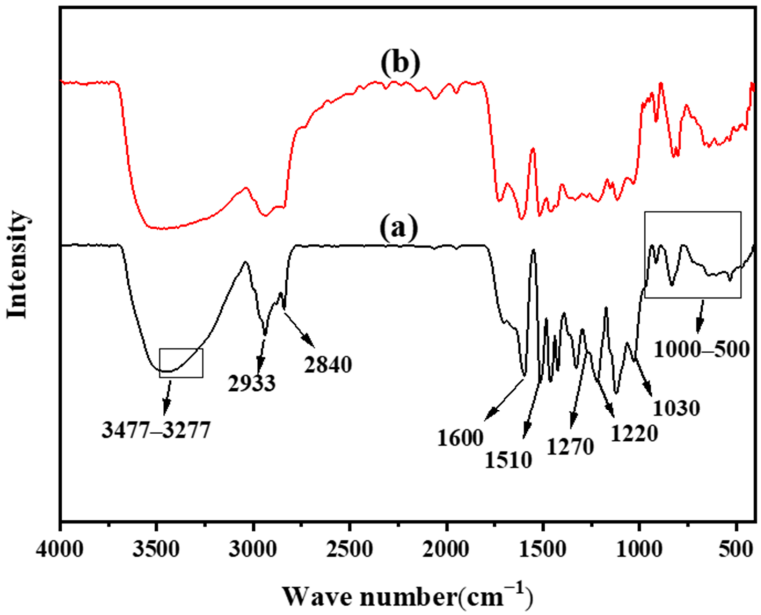

Figure 8. FT-IR characterization of natural lignin and hydrogenolysis liquid products: (a) pristine lignin and (b) Cu-Pd@SNCB catalyst depolymerization products. Reaction conditions: lignin, 0.2 g; solvent methanol, 35 mL; hydrogen pressure, 2 MPa; reaction temperature, 270 °C; reaction time, 3 h.

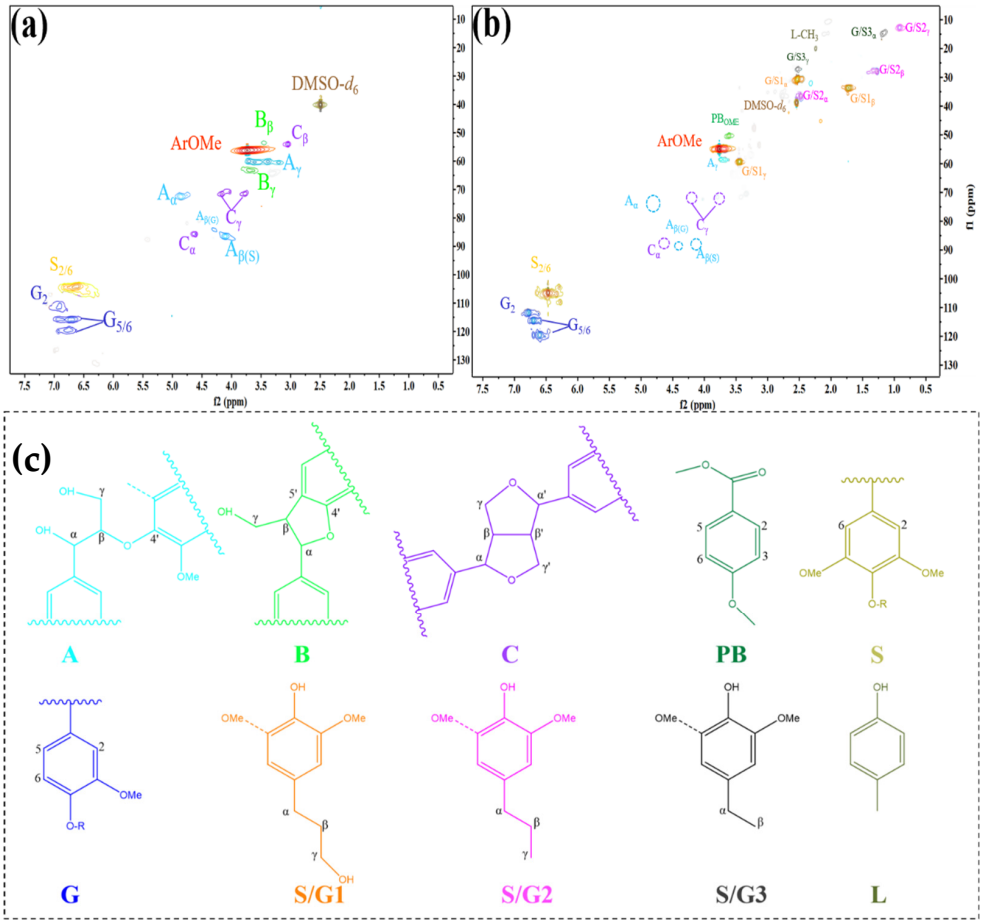

Figure 9. Two-dimensional HSQC NMR characterization with (**a**) raw lignin and (**b**) liquid products. Reaction conditions were 0.2 g of lignin and 35 mL of solvent (methanol), 0.1 g of Cu-Pd@SNCB, 2 MPa H_2, 270 °C, 3 h. (**c**) Primary structure exhibited in the 2D HSQC NMR spectra: (A) b-O-4′ alkyl–aryl ether, (B) b-5′ phenylcoumaran, (C) b-b′ resinol, (PB) p-hydroxybenzoates, (S) syringyl units, (G) guaiacyl units, (S1)4-n-propanolsyringol, (S2)4-n-propylsyringol,(G1)4-n-propanolguaiacol, (G2)4-n-propylguaiacol, (S3) 2,6-dimethoxy-4-ethylphenol, (G3) 4-ethylguaiacol, and (L) 4-methyl phenol.

2.5. Mechanism of Lignin Hydrogenolysis

Based on comprehensive experimental evidence, the reaction pathway for lignin hydrodepolymerization over Cu-Pd@SNCB catalysts was proposed [46] (Figure 10). The mechanism involves three critical steps: First, Pd nanoparticles preferentially dissociate molecular hydrogen (or hydrogen donors like methanol) into active hydrogen species. Second, Cu species modulate the electronic environment through charge transfer, thereby facilitating substrate adsorption and intermediate stabilization. This synergistic effect between Pd and Cu enhances both catalytic activity and product selectivity (46.3% for target monomers). Eucalyptus lignin is mainly composed of a β-O-4 unit structure. Methanol is used as the hydrogen donor. Under the condition of catalyst and external hydrogen, the C_β-O and C_α-O bonds in the β-O-4 unit structure are effectively broken through the coordination process at the same time, and the oxygen atom combines with the protons to form a hydroxyl group on Pd active site, C-O bond rupture generates carbocations that undergo reduction by hydrogen atoms activated on the catalyst surface, and the desired monophenol is obtained finally. Under the action of hydrogen, the C_β-C_γ bond in 4-propyl-2-methoxyphenol is further hydrogenated and broken to form 3-methoxy-4-propylphenol. Notably, the Cu-Pd@SNCB catalyst inhibited the unwanted side reactions, thus improving the selectivity of the target products.

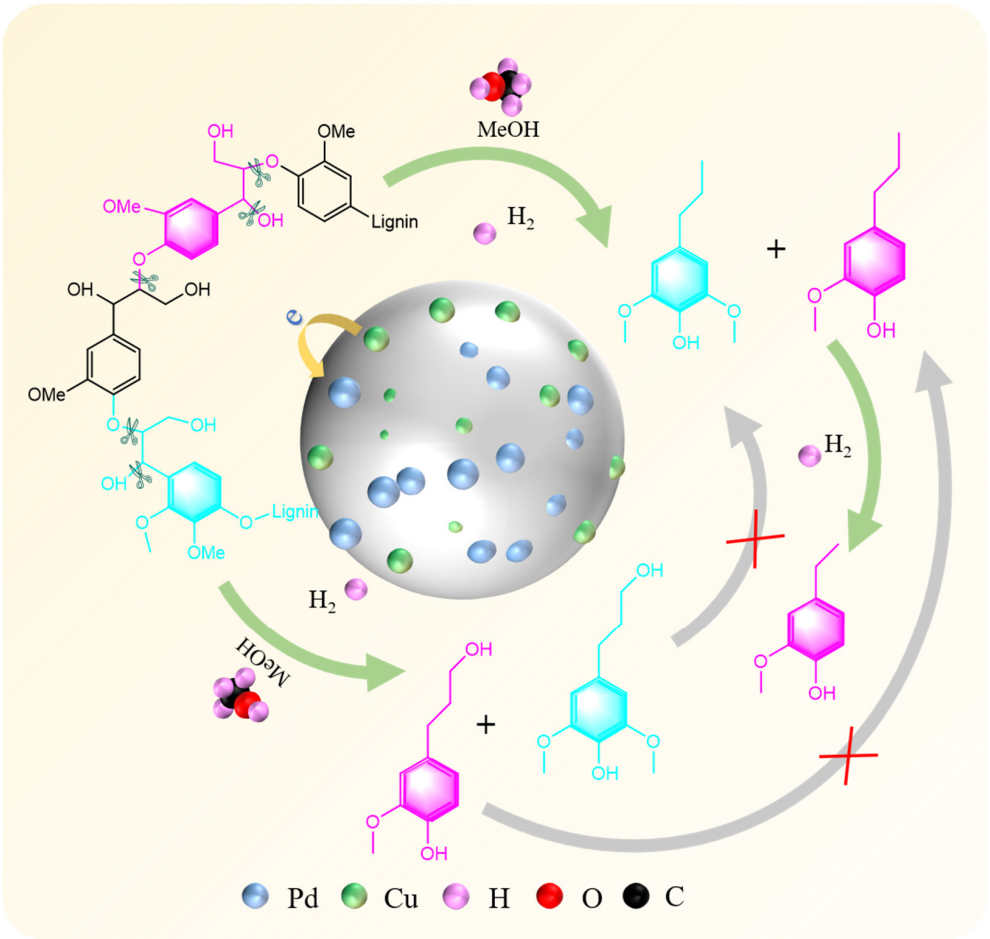

Figure 10. Proposes a mechanistic pathway for lignin hydrogenolysis over Cu-Pd@SNCB catalyst.

3. Experimental Section

3.1. Materials

Organosolv lignin was extracted from eucalyptus wood powder according to the method described in reference [47]. 1,3,5-Homobenzenetricarboxylic acid was sourced from

Shanghai McLean Biochemical Technology (Shanghai, China). Copper chloride dihydrate, methanol solution, ethyl acetate, tetrahydrofuran, sodium hydroxide, and aluminum nitrate hydrate were purchased from Guangzhou Chemical Reagent Factory (Guangzhou, China). Cobalt nitrate hexahydrate was purchased from Tianjin Komeo Chemical Reagen (Tianjin, China). Sodium tetrachloropalladate and sodium borohydride were purchased from Shanghai Aladdin Biochemical Technology (Shanghai, China). Anhydrous ethanol and n-dodecane were provided by Sinopharm Chemical Reagent (Shanghai, China). Nitrogen, argon and hydrogen were purchased from Guangzhou Shengying Gas Company (Guangzhou, China). Detailed information on catalyst characterization can be found in the Supporting Information.

3.2. Catalyst Preparation

3.2.1. Preparation of Al/Co-BTC

Solution A was prepared by dissolving $Al(NO_3)_3 \cdot 9H_2O$ (1.50 g) and $Co(NO_3)_2 \cdot 6H_2O$ (1.20 g) in 40 mL deionized water under magnetic stirring at 25 °C for 30 min. Solution B was obtained by ultrasonicating 1,3,5-benzenetricarboxylic acid (1.70 g) in anhydrous ethanol (40 mL) at 90 kHz for 30 min. The solution A was slowly injected into solution B, and the precursor, solution C, was formed after a 30 min ultrasound-assisted reaction. The homogeneous mixture was transferred to a 100 mL PTFE-lined autoclave and subjected to hydrothermal treatment at 170 ± 2 °C for 10 h in a forced convection oven. After the system was cooled naturally, a pink precipitate was obtained by centrifugation (10,000 rpm, 10 min), and the product was purified by washing twice with deionized water and once with anhydrous ethanol, in that order. The final Al/Co-BTC material was freeze-dried at −54 °C under 0.1 mbar for 12 h, yielding a pink porous powder.

3.2.2. Preparation of Al/Co-BTC-Derived Carbon Materials

A homogeneous dispersion was prepared by co-dispersing Al/Co-BTC powder (1.0 g) with melamine (2.0 g, 99%) in anhydrous ethanol (20 mL, 99.8%) under magnetic stirring (500 rpm) at 25 ± 2 °C for 12 h. The precursor was dried under N_2 flow and then subjected to a two-stage pyrolysis in a tubular furnace: (1) heating to 550 °C at 5 °C/min (N_2 atmosphere, 100 mL/min) with a 3 h hold, followed by (2) further heating to 800 °C (heating rate 3 °C/min) for 3 h activation under flowing N_2. The carbonized product was etched with 5 M NaOH (30 mL) in a 100 mL round-bottom flask equipped with a reflux condenser, maintaining at 150 ± 5 °C in a silicone oil bath with vigorous stirring (800 rpm) for 30 min. The product was collected by centrifugation (10,000 rpm, 10 min) and thoroughly washed with deionized water until neutral pH was achieved. The final material was dried in a convection oven at 50 ± 2 °C for 4 h to obtain nitrogen-doped porous carbon, which was labeled as SNCB.

3.2.3. Preparation of Catalyst Cu-Pd@SNCB

Amounts of 0.4000 g of SNCB, 0.0372 g of Na_2PdCl_4, and 0.0730 g of copper(II) chloride dihydrate ($CuCl_2 \cdot 2H_2O$) were mixed in 4 mL of deionized water with continuous stirring for 12 h at room temperature (25 ± 1 °C). A prepared $NaBH_4$ solution ($NaBH_4$:Pd molar ratio = 10) was rapidly injected into the suspension-containing beaker maintained in an ice-water bath (0–4 °C) under vigorous stirring for 3 h. The resulting solid product was sequentially washed with deionized water, collected by centrifugation (8000 rpm, 5 min), and freeze-dried under vacuum at −54 °C for 8 h.

3.3. Hydrogenolysis of Lignin

The lignin hydrogenolysis reaction was performed in a 100 mL autoclave (model AE 100-HTHP, Shanghai Laibei Scientific Instrument Co, Ltd, Shanghai, China.) equipped

with magnetic stirring and temperature control systems. The reaction mixture containing 0.20 g of organosolv lignin, 35.0 mL of methanol, and 0.10 g of catalyst was loaded into the autoclave, followed by three nitrogen purge-evacuation cycles (0.5 MPa N_2, 5 min each) to ensure an oxygen-free atmosphere. Subsequently, 2 MPa H_2 was charged and then heated to 270 °C after checking the gas tightness of the reactor. The reaction was quenched by rapid cooling in an ice-water bath, and the gas was slowly vented through a pressure relief valve before opening the reactor.

3.4. Product Analysis

Hydrolysis products exist mainly in three forms: gaseous, liquid and solid. In this case, the composition of gaseous products was analyzed by gas chromatography (GC, Agilent 7890A, Guangzhou, China). Liquid products obtained by filtration were analyzed by gas chromatography–mass spectrometry (GC-MS, Japan Shimazu QP 2010 Plus, Shimadzu, Japan), where n-dodecane was used as an internal standard. The solids were washed several times with tetrahydrofuran (THF) and the resulting filtrate was rotary evaporated to collect unreacted organic solvent lignin. The washed solids were dried at 60 °C under vacuum until constant weight (±0.1 mg). The char yield was determined gravimetrically by subtracting the catalyst mass from the total solid residue mass.

In addition, the chemical structure of the products was examined using Fourier-transform infrared spectroscopy (FT-IR, Nicolet IS50, Shanghai, China) and gel permeation chromatography (GPC, Waters 2414, Guangzhou, China). The conversion and liquefaction yields of the lignin hydrolysis were calculated from Equations (1) and (2). The yield of phenolic monomers was obtained from Equation (3), and the yield of char from the hydrogenolysis process was calculated from Equation (4).

$$conversion = \frac{m_F - m_R}{m_F} \times 100\% \quad (1)$$

$$yield\ of\ liquefaction = \frac{m_L}{m_F} \times 100\% \quad (2)$$

$$yield\ of\ phenolic\ monomers = \frac{m_P}{m_F} \times 100\% \quad (3)$$

$$yield\ of\ char = \frac{m_C}{m_F} \times 100\% \quad (4)$$

where m_F represents the added organic solvent lignin mass, m_R indicates the residual lignin mass in organic solvent, m_L corresponds to the measured liquid product yield, m_P represents the phenolic monomers mass, and m_C represents the charcoal mass.

4. Conclusions

This study demonstrates the effective hydrodepolymerization of organosolv eucalyptus lignin catalyzed by a Cu-Pd@SNCB bimetallic system. Under optimized conditions (270 °C, 3 h, 2 MPa H_2 in 35 mL methanol), the catalyst achieved 43.02 wt% phenolic monomer yield with 46.3% selectivity toward 4-(3-hydroxypropyl)-2,6-dimethoxyphenol. Comprehensive characterization revealed that the SNCB support facilitates metal anchoring through its hierarchical porous structure, while the Cu-Pd synergy enhances catalytic performance via dual-functional mechanisms: (1) Cu sites preferentially adsorb and activate lignin β-O-4 linkages, and (2) Pd nanoparticles efficiently dissociate H_2 molecules. The catalyst simultaneously cleaves C-O ether and C-C bonds while selectively producing dihydrosinapyl alcohol, which is directly convertible to dihydrosinapic acid—a key NSAID precursor. This dual functionality positions it as a promising candidate for valorizing lignin into aromatic platform chemicals.

Supplementary Materials: The following supporting information can be downloaded at: https://www.mdpi.com/article/10.3390/catal15050455/s1, Figure S1: SEM characterisation:Cu-Pd@SNCB; Figure S2: TEM characterisation of Cu-Pd@SNCB; Figure S3: (a) XRD patterns of fresh and reused Cu-Pd@SNCB catalysts: (a) fresh, (b)reused; Figure S4: The fitted energies for Pd 3d in monometallic and bimetallic catalysts were (c) Pd@SNCB, (d) Cu-Pd@SNCB; Figure S5: N_2 adsorption-desorption isotherm and pore size distribution of Cu-Pd@SNCB; Figure S6: (a) GC-MS spectra of 2-methoxy-4-ethylphenol; (b) GC-MS spectrum of 4-(3-hydroxypropyl)-2,6-dimethoxypheno; Figure S7: Cu-Pd@SNCB catalyst with and without catalyst hydrogenation products; Table S1: Comparison of bimetallic catalyst activity in different works; Table S2: Element content of Cu-Pd@SNCB; Table S3: N_2 adsorption-desorption of Pd@SNCB and Cu-Pd@SNCB catalyst; Table S4: The mean squared error of product yield or selectivity percentage; Table S5: Gas-phase products of lignin hydrogenolysis; Table S6: Average molecular weights of raw lignin and depolymerisation product [25,48–52].

Author Contributions: Conceptualization, W.L.; methodolgy, W.L., Y.F., S.Q. and J.C.; software, W.L. and J.C.; validation, W.L. and S.G.; investigation, W.L. and S.G.; data curation, W.L.; writing—original draft, W.L.; writing—review and editing, J.C.; visualization, W.L.; supervision, Y.F.; project administration, Y.F. and J.C.; funding acquisition, Y.F. and J.C. All authors have read and agreed to the published version of the manuscript.

Funding: This research was funded by the National Natural Science Foundation of China, grant number 22478134.

Data Availability Statement: Data will be made available on request.

Conflicts of Interest: The authors declare no conflicts of interest.

References

1. Qiu, S.; Fu, Y.; Lei, W.; Chang, J. Preparation of nitrogen and sulfur co-doped tubular porous carbon derived from Ceiba speciosa flowers for supercapacitors. *J. Energy Storage* **2025**, *112*, 115536. [CrossRef]
2. Cabral Almada, C.; Kazachenko, A.; Fongarland, P.; Da Silva Perez, D.; Kuznetsov, B.N.; Djakovitch, L. Supported-metal catalysts in upgrading lignin to aromatics by oxidative depolymerization. *Catalysts* **2021**, *11*, 467. [CrossRef]
3. Huang, Z.; Li, X.; Chen, Z.; Li, P.; Ji, X.; Zhi, C. Anion chemistry in energy storage devices. *Nat. Rev. Chem.* **2023**, *7*, 616–631. [CrossRef]
4. Zakzeski, J.; Bruijnincx, P.C.A.; Jongerius, A.L.; Weckhuysen, B.M. The Catalytic Valorization of Lignin for the Production of Renewable Chemicals. *Chem. Rev.* **2010**, *110*, 3552–3599. [CrossRef]
5. Cao, L.; Yu, I.K.M.; Liu, Y.; Ruan, X.; Tsang, D.C.W.; Hunt, A.J.; Ok, Y.S.; Song, H.; Zhang, S. Lignin valorization for the production of renewable chemicals: State-of-the-art review and future prospects. *Bioresour. Technol.* **2018**, *269*, 465–475. [CrossRef] [PubMed]
6. Kumar, A.; Srivastava, R. Selective C-O bond cleavage in diphenyl ether via catalytic transfer hydrogenolysis over Ru-decorated nanocrystalline H-ZSM-5. *Sustain. Energy Fuels* **2023**, *7*, 5714–5732. [CrossRef]
7. Fernández-Rodríguez, J.; Erdocia, X.; Sánchez, C.; González Alriols, M.; Labidi, J. Lignin depolymerization for phenolic monomers production by sustainable processes. *J. Energy Chem.* **2017**, *26*, 622–631. [CrossRef]
8. Wang, H.-M.; Yuan, T.-Q.; Song, G.-Y.; Sun, R.-C. Advanced and versatile lignin-derived biodegradable composite film materials toward a sustainable world. *Green Chem.* **2021**, *23*, 3790–3817. [CrossRef]
9. Guiton, M.; Suárez-Montes, D.; Sánchez, R.; Baustert, P.; Soukoulis, C.; Okan, B.S.; Serchi, T.; Cambier, S.; Benetto, E. Comparative Life Cycle Assessment of a microalgae-based oil metal working fluid with its petroleum-based and vegetable-based counterparts. *J. Clean. Prod.* **2022**, *338*, 130506. [CrossRef]
10. Nargotra, P.; Sharma, V.; Wang, H.-M.D.; Shieh, C.-J.; Liu, Y.-C.; Kuo, C.-H. Biocatalysis for lignin conversion and valorization: Driving sustainability in the circular economy. *Catalysts* **2025**, *15*, 91. [CrossRef]
11. Xu, Y.; Liu, L.; Xu, Y.; Yan, X.; Zhang, C.; Sun, Z.; Lin, X.; Duan, Y.; Zhang, H. Ultralow loaded waste polystyrene derived hyper-cross-linked polymer for incineration flue gas demercuration: Synergistic effect of transition metal and halogen species. *Chem. Eng. J.* **2023**, *471*, 144732. [CrossRef]
12. Stepacheva, A.A.; Manaenkov, O.V.; Markova, M.E.; Sidorov, A.I.; Bykov, A.V.; Sulman, M.G.; Kiwi-Minsker, L. Lignin hydrogenolysis over bimetallic Ni–Ru nanoparticles supported on SiO_2@HPS. *Catalysts* **2023**, *13*, 856. [CrossRef]
13. Yan, J.; Meng, Q.; Shen, X.; Chen, B.; Sun, Y.; Xiang, J.; Liu, H.; Han, B. Selective valorization of lignin to phenol by direct transformation of C_{sp2}–C_{sp3} and C-O bonds. *Sci. Adv.* **2020**, *6*, eabd1951. [CrossRef]

14. Shukla, R.K.; Chaturvedi, A.K.; Volla, C.M.R. Catalytic Cascade Cyclization and Regioselective Hydroheteroarylation of Unactivated Alkenes. *ACS Catal.* **2021**, *11*, 7750–7761. [CrossRef]
15. Qian, Y.; Wei, C.; Tian, Y.; Xi, B.; Xiong, S.; Feng, J.; Qian, Y. Constructing ultrafine lithiophilic layer on MXene paper by sputtering for stable and flexible 3D lithium metal anode. *Chem. Eng. J.* **2021**, *421*, 129685. [CrossRef]
16. Xiao, Z.; Shen, J.; Zhang, J.; Li, D.; Li, Y.; Wang, X.; Zhang, Z. Intermediate stabilization for tuning photocatalytic selective oxidation of CH_4 to CH_3OH over Co_3O_4/ZnO. *J. Catal.* **2022**, *413*, 20–30. [CrossRef]
17. Meng, H.; Yang, Y.; Shen, T.; Yin, Z.; Wang, L.; Liu, W.; Yin, P.; Ren, Z.; Zheng, L.; Zhang, J.; et al. Designing Cu0−Cu+ dual sites for improved C−H bond fracture towards methanol steam reforming. *Nat. Commun.* **2023**, *14*, 7980. [CrossRef] [PubMed]
18. Sun, C.N.; Qu, Y.B.; Wang, Z.L.; Jiang, Q. Hydrogen spillover in alkaline solutions for effective nitrogen fixation. *Chem. Eng. J.* **2023**, *471*, 144589. [CrossRef]
19. Liu, Z.; Yan, T.; Shi, H.; Pan, H.; Kang, P. Grafting amine-functionalized ligand layer on catalyst for electrochemical CO_2 capture and utilization. *Appl. Catal. B Environ.* **2024**, *343*, 123456. [CrossRef]
20. Diao, Z.J.; Huang, L.Q.; Chen, B.; Gao, T.; Cao, Z.Z.; Ren, X.D.; Zhao, S.J.; Li, S. Amorphous Ni-Ru bimetallic phosphide composites as efficient catalysts for the hydrogenolysis of diphenyl ether and lignin. *Fuel* **2022**, *324*, 124489. [CrossRef]
21. Wen, S.; Huang, J.; Li, T.; Chen, W.; Chen, G.; Zhang, Q.; Zhang, X.; Qian, Q.; Ostrikov, K.K. Multiphase nanosheet-nanowire cerium oxide and nickel-cobalt phosphide for highly-efficient electrocatalytic overall water splitting. *Appl. Catal. B Environ.* **2022**, *316*, 121678. [CrossRef]
22. De Falco, A.; Caruso, F.; Su, X.-D.; Iavarone, A.; Ceccarelli, M. A variational algorithm to detect the clonal copy number substructure of tumors from scRNA-seq data. *Nat. Commun.* **2023**, *14*, 1074. [CrossRef]
23. Lin, F.; Ma, Y.; Sun, Y.; Zhao, K.; Gao, T.; Zhu, Y. Heterogeneous Ni–Ru/H-ZSM-5 one-pot catalytic conversion of lignin into monophenols. *Renew. Energy* **2021**, *170*, 1070–1080. [CrossRef]
24. Hu, J.; Zhao, M.; Jiang, B.; Wu, S.; Lu, P. Catalytic Transfer Hydrogenolysis of Native Lignin to Monomeric Phenols over a Ni–Pd Bimetallic Catalyst. *Energy Fuels* **2020**, *34*, 9754–9762. [CrossRef]
25. Zeng, Z.; Xie, J.; Guo, Y.; Rao, R.; Chen, B.; Cheng, L.; Xie, Y.; Ouyang, X. Hydrogenolysis of lignin to produce aromatic monomers over FePd bimetallic catalyst supported on HZSM-5. *Fuel Process. Technol.* **2021**, *213*, 106713. [CrossRef]
26. Zou, W.; Li, H.; Liu, M.; Lv, Y. High-performance depolymerization of lignin by bimetallic Cu-Ni@C catalysts prepared with MOF as a carrier under mild conditions. *Appl. Catal. A Gen.* **2023**, *656*, 119120. [CrossRef]
27. Huang, X.; Korányi, T.I.; Boot, M.D.; Hensen, E.J.M. Catalytic Depolymerization of Lignin in Supercritical Ethanol. *ChemSusChem* **2014**, *7*, 2276–2288. [CrossRef]
28. Yangcheng, R.; Li, J.; He, J.; Zheng, Y.; Yu, H.; Chen, C.; Wang, J. Carboxyl-Decorated UiO-66 Supporting Pd Nanoparticles for Efficient Room-Temperature Hydrodeoxygenation of Lignin Derivatives. *Small* **2024**, *20*, 2309821. [CrossRef] [PubMed]
29. Wang, X.; Meng, Q.; Gao, L.; Liu, J.; Ge, J.; Liu, C.; Xing, W. Metal organic framework derived nitrogen-doped carbon anchored palladium nanoparticles for ambient temperature formic acid decomposition. *Int. J. Hydrogen Energy* **2019**, *44*, 28402–28408. [CrossRef]
30. Wang, Z.; Chen, X.; Sun, Y.; Hua, D.; Yang, S.; Sun, L.; Li, T.; Chen, L. Co-pyrolysis induced strong metal-support interaction in N-doped carbon supported Ni catalyst for the hydrogenolysis of lignin. *Chem. Eng. J.* **2023**, *473*, 145182. [CrossRef]
31. Duan, J.; Liang, Q.; Fu, Y.; Chang, J. Sea urchin-like nitrogen doped hierarchically carbon materials derived from bimetallic-MOF for fast and efficient hydrogen production of formic acid. *Fuel* **2024**, *361*, 130674. [CrossRef]
32. Hambly, B.; Guzinski, M.; Perez, F.; Pendley, B.; Lindner, E. Deposition of EDOT-Decorated Hollow Nanocapsules into PEDOT Films for Optical and Electrochemical Sensing. *ACS Appl. Nano Mater.* **2020**, *3*, 6328–6335. [CrossRef]
33. Zhao, C.; Wang, Y.; Li, Z.; Chen, W.; Xu, Q.; He, D.; Xi, D.; Zhang, Q.; Yuan, T.; Qu, Y.; et al. Solid-Diffusion Synthesis of Single-Atom Catalysts Directly from Bulk Metal for Efficient CO_2 Reduction. *Joule* **2019**, *3*, 584–594. [CrossRef]
34. He, L.; Weniger, F.; Neumann, H.; Beller, M. Synthesis, Characterization, and Application of Metal Nanoparticles Supported on Nitrogen-Doped Carbon: Catalysis beyond Electrochemistry. *Angew. Chem. Int. Ed.* **2016**, *55*, 12582–12594. [CrossRef]
35. Li, F.; Zhu, W.; Jiang, S.; Wang, Y.; Song, H.; Li, C. Catalytic transfer hydrogenation of furfural to furfuryl alcohol over Fe3O4 modified Ru/Carbon nanotubes catalysts. *Int. J. Hydrogen Energy* **2020**, *45*, 1981–1990. [CrossRef]
36. Su, C.; Cheng, H.; Li, W.; Liu, Z.; Li, N.; Hou, Z.; Bai, F.; Zhang, H.; Ma, T. Atomic Modulation of FeCo–Nitrogen–Carbon Bifunctional Oxygen Electrodes for Rechargeable and Flexible All-Solid-State Zinc–Air Battery. *Adv. Energy Mater.* **2017**, *7*, 1602420. [CrossRef]
37. Sun, H.; Wang, G.; Ge, J.; Wei, N.; Sui, W.; Chen, Z.; Jia, H.; Parvez, A.M.; Si, C. Reduction of lignin heterogeneity for improved catalytic performance of lignin nanosphere supported Pd nanoparticles. *Ind. Crops Prod.* **2022**, *180*, 114685. [CrossRef]
38. Li, L.; Kong, J.; Zhang, H.; Liu, S.; Zeng, Q.; Zhang, Y.; Ma, H.; He, H.; Long, J.; Li, X. Selective aerobic oxidative cleavage of lignin CC bonds over novel hierarchical Ce-Cu/MFI nanosheets. *Appl. Catal. B Environ.* **2020**, *279*, 119343. [CrossRef]
39. Mauriello, F.; Paone, E.; Pietropaolo, R.; Balu, A.M.; Luque, R. Catalytic transfer hydrogenolysis of lignin-derived aromatic ethers promoted by bimetallic pd/Ni systems. *ACS Sustain. Chem. Eng.* **2018**, *6*, 9269–9276. [CrossRef]

40. Wang, M.; Ma, D. Upcycling contaminated plastics. *Nat. Sustain.* **2023**, *6*, 1151–1152. [CrossRef]
41. Sun, Z.; Fridrich, B.; de Santi, A.; Elangovan, S.; Barta, K. Bright Side of Lignin Depolymerization: Toward New Platform Chemicals. *Chem. Rev.* **2018**, *118*, 614–678. [CrossRef] [PubMed]
42. Shuai, L.; Amiri, M.T.; Questell-Santiago, Y.M.; Héroguel, F.; Li, Y.; Kim, H.; Meilan, R.; Chapple, C.; Ralph, J.; Luterbacher, J.S. Formaldehyde stabilization facilitates lignin monomer production during biomass depolymerization. *Science* **2016**, *354*, 329–333. [CrossRef] [PubMed]
43. Jiang, W.; An, Y.; Wang, Z.; Wang, M.; Bao, X.; Zheng, L.; Cheng, H.; Wang, P.; Liu, Y.; Zheng, Z.; et al. Stress-induced BiVO4 photoanode for enhanced photoelectrochemical performance. *Appl. Catal. B Environ.* **2022**, *304*, 121012. [CrossRef]
44. Kaiho, A.; Kogo, M.; Sakai, R.; Saito, K.; Watanabe, T. In situ trapping of enol intermediates with alcohol during acid-catalysed de-polymerisation of lignin in a nonpolar solvent. *Green Chem.* **2015**, *17*, 2780–2783. [CrossRef]
45. Questell-Santiago, Y.M.; Galkin, M.V.; Barta, K.; Luterbacher, J.S. Stabilization strategies in biomass depolymerization using chemical functionalization. *Nat. Rev. Chem.* **2020**, *4*, 311–330. [CrossRef]
46. Yang, C.; Zhuang, C.; Zhai, Z.; Zhao, X.; Huang, D.; Tian, D.; Min, C.; Zhao, J.; Wang, Y. Phase regulation of Ni-based catalyst promotes selective hydrogenation of furfural: Effect of glycerol and Zn content. *Appl. Catal. B Environ.* **2023**, *334*, 122854. [CrossRef]
47. Liang, Q.; Fu, Y.; Qiu, S.; Chang, J. Sustainable Production of High-Value Chemicals from Selective Hydrogenolysis of Lignin Catalyzed by Co–Pd Bimetallic Supported on Nitrogen-Doped Carbon Spheres. *Energy Fuels* **2024**, *38*, 10993–11005. [CrossRef]
48. Van den Bosch, S.; Renders, T.; Kennis, S.; Koelewijn, S.F.; Van den Bossche, G.; Vangeel, T.; Deneyer, A.; Depuydt, D.; Courtin, C.M.; Thevelein, J.M.; et al. Integrating lignin valorization and bio-ethanol production: On the role of Ni-Al_2O_3 catalyst pellets during lignin-first fractionation. *Green Chem.* **2017**, *19*, 3313–3326. [CrossRef]
49. Wang, S.; Xing, Y.; Xu, H.; Zhang, S. MnO nanoparticles interdispersed in 3D porous carbon framework for high performance lithium-ion batteries. *ACS Appl. Mater. Interfaces* **2014**, *6*, 12713–12718. [CrossRef]
50. Yan, B.; Lin, X.; Chen, Z.; Cai, Q.; Zhang, S. Selective production of phenolic monomers via high efficient lignin depolymerization with a carbon based nickel-iron-molybdenum carbide catalyst under mild conditions. *Bioresour. Technol.* **2021**, *321*, 124503. [CrossRef]
51. Shu, R.; Zhou, L.; Zhu, Z.; Luo, B.; You, H.; Zhong, Z.; He, Y. Enhanced hydrogenolysis of enzymatic hydrolysis lignin over in situ prepared RuNi bimetallic catalyst. *Int. J. Hydrogen Energy* **2022**, *47*, 41564–41572. [CrossRef]
52. Gao, X.; Zhu, S.; Li, Y. Selective hydrogenolysis of lignin and model compounds to monophenols over AuPd/CeO_2. *Mol. Catal.* **2019**, *462*, 69–76. [CrossRef]

Disclaimer/Publisher's Note: The statements, opinions and data contained in all publications are solely those of the individual author(s) and contributor(s) and not of MDPI and/or the editor(s). MDPI and/or the editor(s) disclaim responsibility for any injury to people or property resulting from any ideas, methods, instructions or products referred to in the content.